

Influence of anti-site disorder and electron-electron correlations on the electronic structure of CeMnNi₄

Pampa Sadhukhan^{1,†}, Sunil Wilfred D'Souza^{1,†*}, Vipin Kumar Singh¹, Rajendra Singh Dhaka^{1a}, Andrei Gloskovskii², Sudesh Kumar Dhar³, Pratap Raychaudhuri³, Ashish Chainani⁴, Aparna Chakrabarti^{5,6}, Sudipta Roy Barman¹

¹UGC-DAE Consortium for Scientific Research, Khandwa Road, Indore 452001, Madhya Pradesh, India

²Deutsches Elektronen-Synchrotron DESY, Notkestrasse 85, D-22607 Hamburg, Germany

³Department of Condensed Matter Physics and Materials Science,

Tata Institute of Fundamental Research, Homi Bhabha Road, Colaba, Mumbai 400005, India

⁴National Synchrotron Radiation Research Center, Hsinchu 30076, Taiwan

⁵Theory and Simulations Laboratory, Raja Ramanna Centre for Advanced Technology, Indore, 452013, India

⁶Homi Bhabha National Institute, Anushakti Nagar, Mumbai, 400094, India and

[†]The authors have contributed equally to this work.

CeMnNi₄ exhibits an unusually large spin polarization, but its origin has baffled researchers for more than a decade. We use bulk sensitive hard x-ray photoelectron spectroscopy (HAXPES) and density functional theory based on the Green's function technique to demonstrate the importance of electron-electron correlations of both the Ni 3d (U_{Ni}) and Mn 3d (U_{Mn}) electrons in explaining the valence band of this multiply correlated material. We show that Mn-Ni anti-site disorder as well as U_{Ni} play crucial role in enhancing its spin polarization: anti-site disorder broadens a Ni 3d minority-spin peak close to the Fermi level (E_F), while an increase in U_{Ni} shifts it towards E_F , both leading to a significant increase of minority-spin states at E_F . Furthermore, rare occurrence of a valence state transition between the bulk and the surface is demonstrated highlighting the importance of HAXPES in resolving the electronic structure of materials unhindered by surface effects.

In recent years, hard x-ray photoelectron spectroscopy (HAXPES) has turned out to be a reliable tool to study the electronic structure of correlated systems, thin films and buried interfaces of materials, thus providing new insights into their physical properties¹⁻³. In this work, we present the first study of the electronic structure of CeMnNi₄, an interesting material with large spin transport polarization of 66%⁴, using HAXPES and density functional theory calculations based on the spin polarized relativistic Korringa-Kohn-Rostoker (SPRKKR) method⁵. CeMnNi₄ has a cubic MgCu₄Sn-type structure⁶; it is ferromagnetic with a magnetic moment of $4.95\mu_B$ and Curie temperature of 140 K⁴. These encouraging properties of CeMnNi₄ started a flurry of activity aimed at understanding its electronic structure⁷⁻⁹. However, no photoemission study of its electronic structure has been reported to date, and the theoretical studies so far have been unable to explain the different aspects of its electronic structure and its spin polarization in particular. The early density functional theory (DFT) calculations⁷ reported a spin polarization¹⁰ (P_0) value of about 16-20%; and the much larger experimental polarization was attributed to disorder or non-stoichiometry of the specimens. In fact, in a subsequent x-ray absorption fine structure (XAFS) study, about 6% Mn-Ni anti-site disorder was reported⁸. The authors also performed a DFT calculation using the pseudopotential method as implemented in the VASP code including an ordered anti-site defect configuration of nearest neighbour Ni and Mn that were site-exchanged. Thus, in this approach, the effect of randomly disordered anti-site defects is not taken into account. Their results however showed a significant increase in P_0 , which was not related to disorder, but rather to enhanced minority spin states of the site-

exchanged Mn 3d partial density of states (PDOS) due to hybridization with neighboring Ni atom⁸. On the other hand, another DFT calculation that considered electron-electron correlation of the Mn 3d electrons (U_{Mn}) but no anti-site defect showed that P_0 increases with U_{Mn} ⁹. In the absence of any photoemission study and its direct comparison with theory that addresses the influence of both anti-site disorder and correlation, their role in determining the electronic structure and spin polarization of CeMnNi₄ has remained an unresolved question until date.

In this letter, we show that both anti-site disorder and electron-electron correlations for Ni 3d (U_{Ni}) and Mn 3d (U_{Mn}) electrons have a crucial influence on the bulk electronic structure of CeMnNi₄. In addition, since U_{Ce} is typically taken to be about 7 eV in Ce intermetallics¹¹, CeMnNi₄ can be regarded as a multiply correlated system, further complicated by the presence of inherent disorder⁸. U_{Ni} and U_{Mn} are responsible for determining the energy positions of the peaks in the valence band (VB) and their optimum values ($U_{Mn}=4.5$ eV, $U_{Ni}=6.5$ eV) are obtained by the best agreement between theoretically calculated and the experimental HAXPES VB. A surprising result is that the large P_0 of CeMnNi₄ has two origins: the anti-site disorder (x) and U_{Ni} . The former broadens a minority spin Ni 3d peak close to E_F , while the latter shifts it towards E_F . Thus, in both cases, the minority spin total DOS at E_F ($n_{\downarrow}(E_F)$) increases, while the majority spin total DOS ($n_{\uparrow}(E_F)$) remains essentially unchanged, resulting in a clear enhancement of P_0 . The total magnetic moment exhibits contrasting variation: a decrease with x and an increase with U_{Ni} . Furthermore, rare occurrence of a valence state transition on the surface of a ternary

material is demonstrated: a bulk mixed valent state transforms to a nearly trivalent Ce^{3+} state due to the weakened hybridization on the surface.

Experimental and computational methods:

HAXPES measurements were performed at the P09 beamline in PETRA III synchrotron center, Germany on polycrystalline $CeMnNi_4$ ingot that was cleaved under ultra high vacuum at 2×10^{-8} mbar pressure to expose a fresh surface. The spectra were recorded by using Phoibos 225 analyzer with 30 eV pass energy at 50 K¹². Photons were incident on the sample at a grazing angle (10°) and the photoelectrons were collected in the nearly normal emission geometry. The total instrumental resolution (including both source and analyzer contributions), obtained from the least square fitting of the Au Fermi edge in electrical contact with the specimen, is 0.26 eV. $CeMnNi_4$ ingot was prepared by an arc melting method and characterized for its structure using x-ray diffraction, as discussed in Ref. 4.

The bulk ground state properties of $CeMnNi_4$ have been calculated in $F\bar{4}3m$ symmetry using the experimental lattice parameter ($a = 6.9706 \text{ \AA}$) as determined by neutron powder diffraction at 17 K⁶. Disordered Mn-Ni anti-site defects have been considered by setting the 16e site occupations to $1-0.25x$ for Ni_{Ni} and $0.25x$ for Mn_{Ni} , while the occupancies at the 4c site were set to $1-x$ for Mn_{Mn} and x for Ni_{Mn} , where X_Z refers to a X atom at a Z atom site (X, Z= Ni, Mn). Here, x quantifies the amount of anti-site disorder as the fraction of Mn atoms occupying the Ni sites. In this work, we have varied x from 0 to 0.12. The structures are shown in Fig. S1 of SM.

Self-consistent band structure calculations were carried out using fully relativistic SPRKKR method in the atomic sphere approximation⁵. The exchange and correlation effects were incorporated within the generalized gradient approximation framework.¹³ The electron-electron correlation has been taken into account as described in the LSDA+U scheme¹⁴. The parameters of screened on-site Coulomb interaction U for all the components (U_{Ni} , U_{Mn} and U_{Ce}) have been varied up to 7 eV, with the exchange interaction J fixed at 0.8 eV. The static double counting of LSDA+U approach has been corrected using the atomic limit scheme. The angular momentum expansion up to $l_{max} = 4$ has been used for each atom. The energy convergence criterion and coherent potential approximation tolerance has been set to 10^{-5} Ry. Brillouin zone integrations were performed on a $36 \times 36 \times 36$ mesh of k -points in the irreducible wedge of the Brillouin zone. We have employed Lloyd's formula, which provides an accurate determination of the Fermi level and density of states¹⁵. For calculating the angle integrated VB spectrum, all the PDOS contributions from s , p , d and f states of Ce, Mn and Ni were multiplied with their corresponding photoemission cross-sections¹⁶ and then added. This is multiplied by the Fermi function and convoluted with the instrumental resolution and an

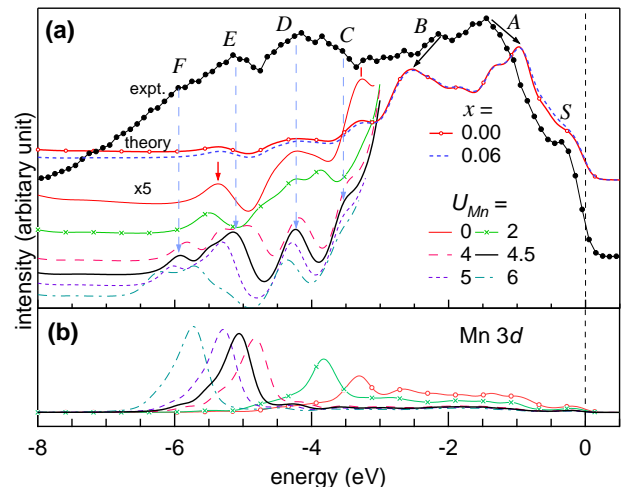


Figure 1: (a) The valence band (VB) HAXPES spectra of $CeMnNi_4$ at 50 K using 8 keV photon energy (black filled circles) compared with the calculated VB spectra for $x = 0$ (no disorder) and $x = 0.06$ (6% Mn-Ni anti-site disorder). The VB's calculated with different U_{Mn} are shown in the -3 to -8 eV range, where $x = 0$, $U_{Ni} = U_{Ce} = 0$ eV. The spectra are staggered along the vertical axis, zero of the horizontal scale corresponds to the Fermi level (E_F). (b) Mn 3d contribution to the calculated VB as a function of U_{Mn} .

energy dependent lifetime broadening $0.01 \times (E_B - E_F)^{17}$ to obtain the VB.

Valence band of $CeMnNi_4$: The VB spectrum recorded with 8 keV photon energy at 50 K shows a step (S) close to E_F at -0.4 eV; peaks at -1.5 (A), -2.2 (B), -3.6 (C), -4.2 (D), -5.2 eV (E) and a weak shoulder at -6 eV (F) (Fig. 1(a)). In order to ascertain their origin and study the influence of disorder on the spectral shape, we have calculated the VB spectra without (red line with open circles, $x = 0$) and with 6% Mn-Ni anti-site disorder (blue dashed line, $x = 0.06$). 6% disorder is considered because a previous XAFS study⁸ inferred a disorder of this magnitude on a specimen that was prepared by the same procedure as ours. As discussed above, the VB has been calculated from the partial DOS (PDOS) in Fig. S2. We find that disorder results in a small but finite broadening of the VB, but it has no effect on the position of the peaks. Comparison of the calculated VB with HAXPES shows glaring differences: the peaks corresponding to A and B (black arrows) are positioned at higher and lower energies, respectively and thus their separation (1.6 eV) is significantly larger compared to experiment (0.7 eV). The peak at -5.4 eV (red arrow) is shifted *w.r.t.* peak E of the experimental VB, the peak at -3.3 eV (red tick) appears at a dip, while there is no peak in the theory corresponding to F (see the blue dashed arrows). In Fig. S2, DOS calculated with disorder up to $x = 0.12$ (*i.e.* 12% anti-site disorder) show increased broadening, but the positions of all the peaks remain unchanged.

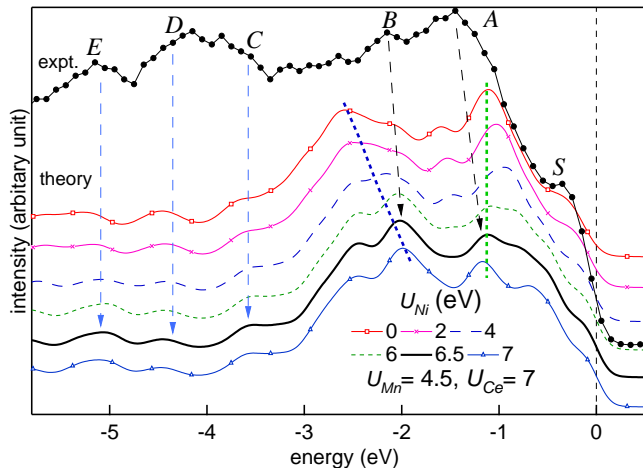


Figure 2: The valence band HAXPES spectrum of Fig. 1 (black filled circles) compared with calculated VB spectra as a function of U_{Ni} , with $U_{Mn} = 4.5$ eV, $U_{Ce} = 7$ eV and $x = 0$.

Thus, it is obvious from the above discussion that disorder is unable to explain the VB. So, we examine the possible role of correlation starting with U_{Mn} . As U_{Mn} is increased, interesting modifications in the -3 to -6 eV region is observed in Fig. 1(a), which are primarily related to the systematic changes in the Mn 3d PDOS (Fig. 1(b) and PDOS in Fig. S3). At $U_{Mn} = 0$, the Mn 3d states are delocalized over 0 to -5 eV with the most intense peak at -3.3 eV. Increase of U_{Mn} narrows the Mn 3d PDOS, the peak intensity increases and it shifts by a large amount to lower energies *i.e.* away from E_F (*e.g.* -5.2 eV for $U_{Mn} = 4.5$ eV). The best agreement with experiment in the -3 to -6 eV region is obtained for $U_{Mn} = 4.5$ eV (black line), where the peaks at -3.6, -4.2, -5.2 and -6 eV appear at the same positions as C, D, E, and F, respectively of the experimental VB, as shown by the blue dashed arrows in Fig. 1(a). The Mn 3d states contribute primarily to the peak E, however, its intensity is relatively less due to smaller photoemission cross-section of Mn 3d with respect to Ni 3d at 8 keV¹⁶.

Although $U_{Mn} = 4.5$ eV provides a good agreement for peaks C-F, the positions of the peaks A and B are not well reproduced, and these remain unaltered with U_{Mn} (Fig. S3). It is evident that A and B originate primarily from Ni 3d states, and so we calculate the VB by introducing U_{Ni} , with U_{Mn} fixed at 4.5 eV. We find that as U_{Ni} increases, the peak at -2.6 eV shifts to higher energy *i.e.* towards E_F (blue dashed line) and appears close to the position of peak B for $U_{Ni} = 6.5$ eV (Fig. 2, see Fig. S4 for PDOS). On the other hand, the peak at -1.1 eV initially shifts to higher energies and eventually shifts back to lower energy (green dashed line) towards peak A. The separation of these two peaks is lowest (0.8 eV) at $U_{Ni} = 7$ eV. However, for $U_{Ni} = 7$ eV, a new peak appears at -0.7 eV in disagreement with experiment. Thus, we con-

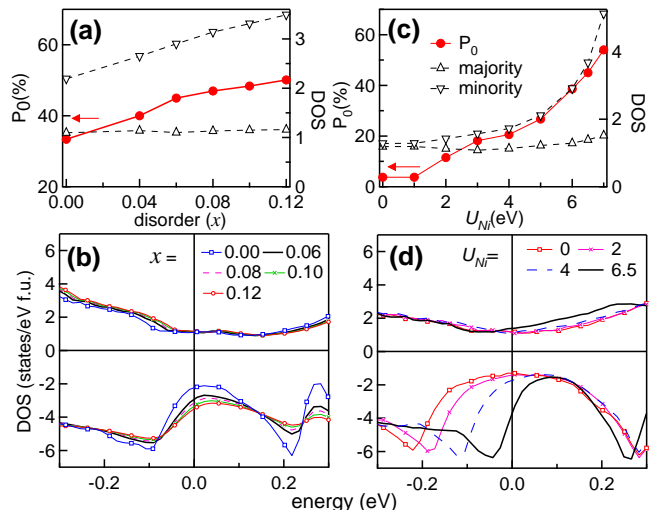


Figure 3: Spin polarization (P_0), majority ($n_{\uparrow}(E_F)$) and minority ($n_{\downarrow}(E_F)$) spin total DOS at E_F (a) as a function of disorder (x) with $U_{Ni} = U_{Mn} = U_{Ce} = 0$; and (c) as a function of U_{Ni} , where $U_{Mn} = 4.5$ eV, $U_{Ce} = 7$ eV and $x = 0$. Majority and minority spin total DOS around E_F corresponding to (a) and (c) as a function of (b) x and (d) U_{Ni} , respectively.

clude that the best agreement is observed for $U_{Ni} = 6.5$ eV, where the positions as well as the separation (0.9 eV) of the calculated peaks agree well with A and B (black dashed arrows in Fig. 2). Note that the peaks in the -3 to -6 eV region are hardly affected by U_{Ni} .

It is to be noted that in Fig. 2 we also consider a value of $U_{Ce} (= 7$ eV) for the Ce 4f electrons that is generally observed in Ce intermetallic compounds¹¹. However, U_{Ce} does not have any discernible effect on the occupied states and the VB, since the Ce 4f peak appears mostly above E_F at 0.9 eV for $U_{Ce} = 0$ (Fig. S3(c)) and shifts to higher energy (1.2 eV) for $U_{Ce} = 7$ eV (Fig. S4(a)). Thus, due to the significant variation of Ni and Mn 3d states with U_{Ni} and U_{Mn} , respectively and taking U_{Ce} from literature¹¹, we are able to determine the optimum values of U for CeMnNi₄ to be: $U_{Mn} = 4.5$ eV, $U_{Ni} = 6.5$ eV and $U_{Ce} = 7$ eV (referred henceforth as $U(4.5, 6.5, 7)$). The partial contributions of the different PDOS to each of the peaks in the VB for $U(4.5, 6.5, 7)$ are shown in Fig. S5 of SM.

Spin polarization and magnetic moments: We find that the Mn-Ni anti-site disorder has an unexpected positive effect on the spin polarization (P_0). As shown in Fig. 3(a) and Table I of SM, P_0 exhibits a monotonic increase with x , reaching a value of 45% (50%) for $x = 0.06$ (0.12). This is an important result since in half metals and Heusler alloys, a low experimental value of P_0 is generally attributed to disorder¹⁸. In order to understand the reason for this unusual behavior, we show the spin polarized total DOS around E_F in Fig. 3(b). A peak in the minority spin DOS close to E_F at -0.1 eV

progressively broadens and also shifts by a small amount (≈ 15 meV) towards E_F resulting in increase of $n_{\downarrow}(E_F)$ with x . On the contrary, the structureless majority spin DOS and consequently $n_{\uparrow}(E_F)$ remain almost unchanged. Thus, this contrasting behavior of $n_{\downarrow}(E_F)$ and $n_{\uparrow}(E_F)$ brings about the increase of P_0 with x (Fig. 3(a)). Table I of SM defines and shows the partial contributions from Ni 3d ($P_{0_{\text{Ni}3d}}$), Mn 3d ($P_{0_{\text{Mn}3d}}$) and Ce 4f ($P_{0_{\text{Ce}4f}}$) PDOS to P_0 for different x , and we find that P_0 increases solely because of $P_{0_{\text{Ni}3d}}$. This is also confirmed in Fig. S6 where the peak in the minority spin DOS is clearly dominated by Ni 3d PDOS (black tick).

Turning to the influence of U on P_0 (Fig. 3(c)), we find that it increases with U_{Ni} from about 3.8% for $U(4.5,0,7)$ to 45% for $U_{\text{Ni}}=6.5$ eV *i.e.* for the optimum $U(4.5,6.5,7)$. This is related to increase of $n_{\downarrow}(E_F)$ due to a significant shift of the minority spin total DOS peak towards E_F from -0.2 to -0.05 eV (Fig. 3(d)). Clearly the total DOS is dominated by Ni 3d, black ticks in Fig. S7 show how the minority spin Ni 3d PDOS peak shifts with U_{Ni} . In contrast, the majority spin total DOS is structureless and $n_{\uparrow}(E_F)$ remains almost unchanged (Fig. 3(c,d)). The partial contributions to P_0 for different U_{Ni} clearly show that the increase in P_0 is entirely due to $P_{0_{\text{Ni}3d}}$ (Table I of SM).

Due to disorder, the Ni 3d minority spin peak will broaden and also possibly shift by small amount towards E_F and thus significantly increase $n_{\downarrow}(E_F)$ because of its proximity to E_F (*e.g.* at -0.05 eV for $U(4.5,6.5,7)$). On the other hand, $n_{\uparrow}(E_F)$ would remain unchanged due to the nearly flat nature of the majority spin total DOS. Thus, disorder would further increase P_0 , and assuming that its effect is independent of U , we estimate P_0 for $U(4.5,6.5,7)$ to increase from 45% to >55% (>60%) for $x=0.06$ (0.12). This is in good agreement with the experimental value of 66%, given the fact that the measurements were performed in the diffusive limit⁴ and here we calculate the static spin polarization.

We have also studied how U_{Mn} and U_{Ce} affects P_0 and find that both have detrimental effect: in Fig. 4(a), $P_0(U_{\text{Mn}},0,0)$ shows a decrease from 33.4% to 11.4% with U_{Mn} varying from 0 to 7 eV. In comparison, the effect of U_{Ce} is milder with $P_0(0,0,U_{\text{Ce}})$ decreasing from 33.4% to 28%. If U_{Mn} and U_{Ce} are set to 0, P_0 increases to a large value of 66% for $U_{\text{Ni}}=7$ eV *i.e.* for $U(0,7,0)$ (black filled squares in Fig. 4(a)). On the other hand, a comparison of $P_0(U_{\text{Ni}})$ for $(0,U_{\text{Ni}},0)$, $(5,U_{\text{Ni}},0)$, $(4.5,U_{\text{Ni}},7)$ shows that the extent of increase of P_0 is clearly arrested when U_{Mn} and U_{Ce} are non-zero. These results refute an earlier counterintuitive report⁹, which concluded that U_{Mn} increases P_0 , while neither U_{Ni} nor U_{Ce} have any influence on P_0 (see Supplementary discussion SD1).

The calculated magnetic moments show that the total moment of CeMnNi_4 is quite large *e.g.* $5.43 \mu_B$ for $U(4.5,6.5,7)$, the main contribution coming from the Mn spin moment ($4.31 \mu_B$). Fig. 4(b) shows that both the total moment as well as the Ni spin moment increase with U_{Ni} , *e.g.* for $U(4.5,0,7)$ the total moment (Ni spin

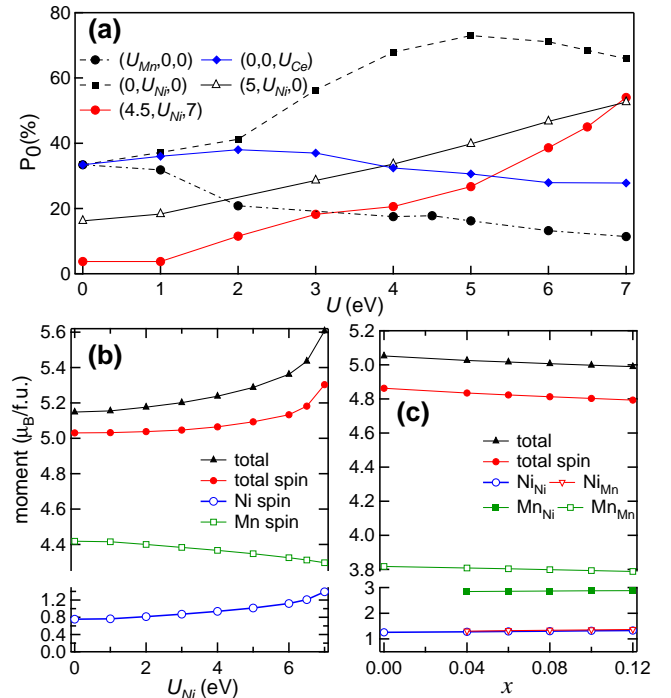


Figure 4: (a) Spin polarization P_0 as a function of electron-electron correlation U for Ni 3d (U_{Ni}), Mn 3d (U_{Mn}) and Ce 4f electrons (U_{Ce}). P_0 is plotted as a function of U shown as a triplet $(U_{\text{Mn}}, U_{\text{Ni}}, U_{\text{Ce}})$, where the fixed U values in the triplet are indicated by numbers in eV. For example, $(5, U_{\text{Ni}}, 0)$ means U_{Ni} varies from 0 to 7 eV with U_{Mn} and U_{Ce} fixed at 5 eV and 0 eV, respectively. The total (spin plus orbital) moment, the total spin only moment of CeMnNi_4 and the local spin magnetic moments of Mn and Ni are plotted (b) as a function of U_{Ni} with $U_{\text{Mn}}=4.5$ eV, $U_{\text{Ce}}=7$ eV and $x=0$; and (c) as a function of disorder (x). In all cases, the Ce atom possess a small opposite moment of $-0.2 \mu_B$.

moment) is 5.15 (0.19) μ_B , whereas for $U(4.5,6.5,7)$ it is 5.43 (0.3) μ_B . The increase in the Ni spin moment is because of the shift of the Ni 3d minority spin states towards E_F (Fig. 3(d)) resulting in a decrease of the integrated occupied minority spin PDOS, while the majority spin PDOS remains largely unchanged. It may be noted that the total moment of $5.43 \mu_B$ for $U(4.5,6.5,7)$ is somewhat overestimated compared to the experimental value of $4.95 \mu_B$ from magnetization measurement at 5 K^4 .

Interestingly, we find that the total magnetic moment decreases with increasing disorder (Fig. 4(c)). This can be ascribed to the difference of the Mn_{Ni} (Mn atom in Ni position) and Mn_{Mn} (Mn atom in Mn position) 3d spin-polarized PDOS, the latter having considerably reduced exchange splitting (Fig. S2). This difference is related to the change in hybridization due to different nearest neighbor configurations (Fig. S1). The local moment of Mn_{Ni} is thus substantially smaller ($2.8 \mu_B$) compared to Mn_{Mn} ($3.8 \mu_B$). Although the local moments hardly vary,

the proportion of Mn_{Ni} increases with x , resulting in a decrease of the total moment. Thus, it can be argued that the overestimation of the total moment by theory with $U(4.5,6.5,7)$ mentioned above could be somewhat compensated by its decrease caused by anti-site disorder.

An additional interesting outcome of our study is the demonstration of a valence state transition *i.e.* a change of the valency of Ce between the bulk and the surface. Valence state transition could significantly alter the surface electronic structure compared to the bulk. It was first reported in Sm metal¹⁹ and later in binary Ce intermetallic compounds²⁰. From the analysis of the Ce 3d core-level spectra using HAXPES and XPS and using a simplified version of the Anderson single-impurity model²¹ proposed by Imer and Wuilloud (IW)¹¹, we show that the Ce 4f occupancy in the ground state (n_f) turns out to be 0.8 in the bulk, indicating a mixed valent state with 20% Ce in f^0 (Ce^{4+}) while 80% in f^1 (Ce^{3+}) configuration, where f^0 and f^1 are the satellite peaks in the Ce 3d spectrum related to $3d^9 4f^0$ and $3d^9 4f^1$ final states, respectively^{22,23}. In contrast, from the surface sensitive Ce 3d XPS spectrum, n_f increases to 0.98 and thus the surface has predominantly $3d^9 4f^1$ (Ce^{3+}) ground state. Thus, in the bulk, the Ce 4f electron transfers to the valence states comprising primarily of Ni 3d states making CeMnNi_4 a mixed valent system with 4f occupancy of $n_f = 0.8$. However, at the surface, the reduced hybridization between the Ce 4f and unsaturated 3d states results in a lowering of the Ce 4f states further below E_F . This increases the occupancy of the Ce 4f level ($n_f = 0.98$) and results in the valence state transition. The detailed discussion on the valence state transition and comparison with surface sensitive XPS is provided in the Supplementary discussion SD2.

In conclusion, we settle the long standing debate about the electronic structure of CeMnNi_4 . We establish

the importance of both anti-site disorder and electron-electron correlation in explaining its intriguing properties. Our work fundamentally alters the general notion that anti-site disorder is detrimental for spin polarization. We hope it will motivate further experimental work on CeMnNi_4 and related materials, mainly because disorder could be controlled and P_0 further enhanced. We find that the total magnetic moment exhibits contrasting behaviour, it decreases with x , but increases with U_{Ni} . A valence state transition that originates due to the weakened hybridization on the surface is demonstrated. Our study highlights the power of HAXPES in combination with density functional theory for clarifying the electronic structure and properties of multiply-correlated materials with inherent anti-site disorder.

Acknowledgments: The experiments were carried out at PETRA III of Deutsches Elektronen-Synchrotron, a member of Helmholtz-Gemeinschaft Deutscher Forschungszentren. Financial support by the Department of Science and Technology, Government of India within the framework of India@DESY collaboration is gratefully acknowledged. We would like to thank W. Drube and C. Narayana for support and encouragement. S.W.D. gratefully acknowledges the financial support from CEDAMNF project (CZ.02.1.01/0.0/0.0/15-003/0000358), New Technologies Research Centre, University of West Bohemia, Czech Republic. A.C. thanks P.A. Naik, A. Banerjee for support and encouragement and the Computer Centre of RRCAT, Indore for providing the computational facility for a part of the work.

**^aPresent addresses:* *New Technologies Research Centre, University of West Bohemia, Univerzitní 8, CZ-306 14 Pilsen, Czech Republic; ^aDepartment of Physics, Indian Institute of Technology Delhi, Hauz Khas, New Delhi 110016, India

¹ C. S. Fadley, J. Electron. Spectros. Relat. Phenom. **178–179**, 2 (2010); K. Kobayashi, Nuc. Instrum. Meth. Phys. Res. A **601**, 32 (2009).
² *Hard X-ray Photoelectron Spectroscopy*, ed. J. C. Woicik, Springer Series in Surface Sciences vol. **59** (Springer International Publishing, Switzerland, 2016).
³ A. X. Gray *et al.*, Nat. Mater. **10**, 759 (2011); Nat. Mater. **11**, 958 (2012); Phys. Rev. Lett. **108**, 257208 (2012); J. Nayak *et al.*, Phys. Rev. Lett. **109**, 216403 (2012); T. Ohtsuki *et al.*, Phys. Rev. Lett. **106**, 047602 (2011); M. Sing *et al.*, Phys. Rev. Lett. **102**, 176805 (2009).
⁴ S. Singh, G. Sheet, P. Raychaudhuri, and S. K. Dhar, Appl. Phys. Lett. **88**, 022506 (2006).
⁵ H. Ebert, D. Ködderitzsch, J. Minár, Rep. Prog. Phys. **74**, 096501 (2011).
⁶ I. Dhiman, A. Das, S. K. Dhar, P. Raychaudhuri, S. Singh, P. Manfrinetti, Solid State Comm. **141**, 160 (2007).
⁷ I. Mazin, Phys. Rev. B **73**, 012415 (2006); E. N. Voloshina, Y. S. Dedkov, M. Richter and P. Zahn, Phys. Rev. B **73**, 144412 (2006).

⁸ D. Lahiri, S. Khalid, P. Modak, P. Raychaudhuri, S. K. Dhar, and S. M. Sharma, Phys. Rev. B **82**, 134424 (2010).
⁹ M. S. Bahramy, P. Murugan, G. P. Das, and Y. Kawazoe, Phys. Rev. B **81**, 165114 (2010).
¹⁰ $P_0 = |[n_{\uparrow}(E_F) - n_{\downarrow}(E_F)] / [n_{\uparrow}(E_F) + n_{\downarrow}(E_F)]|$.
¹¹ J. -M. Imer and E. Wuilloud, Z. Phys. B Condens. Matter **66**, 153 (1987).
¹² A. Gloskovskii, G. Stryganyuk, G. H. Fecher, C. Felser, S. Thiess, H. Schulz-Ritter, W. Drube, G. Berner, M. Sing, R. Claessen, and M. Yamamoto, J. Electron Spectrosc. Relat. Phenom. **185**, 47 (2012).
¹³ J. P. Perdew, K. Burke, M. Ernzerhof, Phys. Rev. Lett. **77**, 3865 (1996).
¹⁴ H. Ebert, A. Perlov, S. Mankovsky, Solid State Commun. **127**, 443 (2003).
¹⁵ P. Lloyd, Proc. Phys. Soc. **90**, 207 (1967); P. Lloyd, P. V. Smith Adv. Phys. **21**, 69 (1972); R. Zeller, J. Phys.: Condens. Matter **20**, 035220 (2008).
¹⁶ J. J. Yeh, I. Lindau, Atomic Data Nucl. Data Tables **32**, 1 (1985).

- ¹⁷ A. Fujimori, F. Minami, Phys. Rev. B **30**, 957 (1984); S. R. Barman, D. D. Sarma, Phys. Rev. B **51**, 4007 (1995).
- ¹⁸ K. Özdoğan, E. Sasioğlu, B. Aktas, I. Galanakis, Phys. Rev. B **74**, 172412 (2006); Y. Miura, K. Nagao, and M. Shirai, Phys. Rev. B **69**, 144413 (2004).
- ¹⁹ G. K. Wertheim and G. Crecelius, Phys. Rev. Lett. **40**, 813 (1978); B. Johansson, Phys. Rev. B **19**, 6615 (1979).
- ²⁰ C. Laubschat, E. Weschke, C. Holtz, M. Domke, O. Strelbel, and G. Kaindl, Phys. Rev. Lett. **65**, 1639 (1990).
- ²¹ O. Gunnarsson and K. Schönhammer, Phys. Rev. B **28**, 4315 (1983).
- ²² F. U. Hillebrecht and J. C. Fuggle, Phys. Rev. B **25**, 3550 (1982).
- ²³ J. C. Fuggle, F. U. Hillebrecht, Z. Zolnierrek, R. Lässer, Ch. Freiburg, O. Gunnarsson, K. Schönhammer, Phys. Rev. B **27**, 7330 (1983).
- ²⁴ S. Doniach and M. Šunjić, J. Phys C **3**, 287 (1970).
- ²⁵ S. Tougaard, Surf. Sci. **216**, 343 (1989).
- ²⁶ M. Yano, A. Sekiyama, H. Fujiwara, Y. Amano, S. Imada, T. Muro, M. Yabashi, K. Tamasaku, A. Higashiya, T. Ishikawa, Y. Ōnuki, and S. Suga, Phys. Rev. B **77**, 035118 (2008).
- ²⁷ M. Sundermann, F. Strigari, T. Willers, J. Weinen, Y. F. Liao, K. -D. Tsuei, N. Hiraoka, H. Ishii, H. Yamaoka, J. Mizuki, Y. Zekko, E. D. Bauer, J. L. Sarrao, J. D. Thompson, P. Lejay, Y. Muro, K. Yutani, T. Takabatake, A. Tanaka, N. Hollmann, L. H. Tjeng, A. Severing, J. Electron Spectros. Relat. Phenom. **209**, 1 (2016).
- ²⁸ S. Tanuma, C. J. Powell, and D. R. Penn, Surf. Intf. Anal. **43**, 689 (2011).

Supplementary material to the paper entitled:

Influence of anti-site disorder and electron-electron correlations on the electronic structure of CeMnNi₄

Pampa Sadhukhan^{1,†}, Sunil Wilfred D'Souza^{1,†*}, Vipin Kumar Singh¹, Rajendra Singh Dhaka^{1a}, Andrei Gloskovskii², Sudesh Kumar Dhar³, Pratap Raichaudhuri³, Ashish Chainani⁴, Aparna Chakrabarti⁵, Sudipta Roy Barman¹

[†]Both the authors have contributed equally to this work.

This Supplementary material contains seven figures (S1 to S7), two tables (TABLE-I and II) and two Supplementary discussions (SD1 and SD2, which include figures S8-S13).

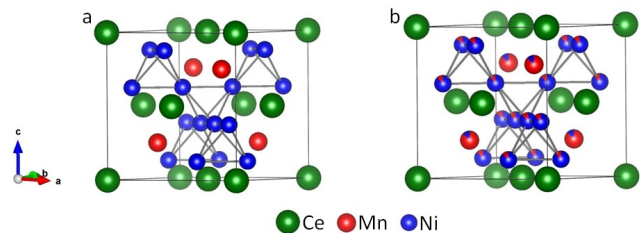


Fig. S 1: The crystal structure of (a) ordered CeMnNi₄ with Ce and Mn are placed at 4a (0, 0, 0) and 4c (0.25, 0.25, 0.25) sites, respectively, while Ni is placed at 16e (0.624, 0.624, 0.624) site. The corresponding multiplicities of 4a, 4c and 16e atomic sites are 1, 1 and 4, respectively and (b) Disordered CeMnNi₄ with 12% ($x=0.12$) Mn-Ni anti-site disorder. The crystallographic axes are represented by the arrows (a, b, c). The entire cubic structure has been rotated by 45° in the clockwise direction to provide a better view. Note that the first nearest neighbor (nn) of Mn_{Mn} (Mn atom in Mn position) are three Ni atoms, while the second nn are four Ce atoms. On the other hand, for Mn_{Ni} (Mn atom in Ni position), the first nn are six Ni atoms, while the second nn are three Mn_{Mn} atoms.

I. SUPPLEMENTARY DISCUSSIONS

A. SD1: Discussion on the spin polarization reported in Ref. 9

Bahrany *et al.*⁹ found the cubic phase of CeMnNi₄ to be stable when U_{Mn} is turned on and reported that the Mn 3d states shift to lower energies with U_{Mn} . We also find similar behavior of the Mn 3d states. However, the authors also reported that the static spin polarization (P_0) increases substantially with U_{Mn} , and commented that U_{Ni} or U_{Ce} have no effect on P_0 or any other ground

TABLE I: The total spin polarization (P_0 , also see Fig. 3 of MS) and the partial contributions to P_0 from the Ni 3d ($P_{0_{\text{Ni}3d}}$), Mn 3d ($P_{0_{\text{Mn}3d}}$) and Ce 4f ($P_{0_{\text{Ce}4f}}$) PDOS, as functions of Mn-Ni anti-site disorder (x) and Ni 3d electron-electron correlation (U_{Ni}). P_0 is calculated using the following formula:

$$P_0 = \left| \frac{n_{\uparrow}(E_F) - n_{\downarrow}(E_F)}{n_{\uparrow}(E_F) + n_{\downarrow}(E_F)} \right|,$$

where $n_{\uparrow}(E_F)$ is the majority spin total DOS at E_F and $n_{\downarrow}(E_F)$ is the minority spin total DOS at E_F . The partial contributions to P_0 from an Xnl PDOS ($P_{0_{Xnl}}$) where $X = \text{Ni, Mn or Ce}$; $n=3-6$; $l = s, p, d$ or f is given by

$$P_{0_{Xnl}} = \left| \frac{n_{\uparrow Xnl}(E_F) - n_{\downarrow Xnl}(E_F)}{n_{\uparrow Xnl}(E_F) + n_{\downarrow Xnl}(E_F)} \right|,$$

where $n_{\uparrow Xnl}(E_F)$ is the majority spin Xnl PDOS at E_F and $n_{\downarrow Xnl}(E_F)$ is the minority spin Xnl PDOS at E_F . Note that $P_0 = \sum_{X,n,l} P_{0_{Xnl}}$, when all possible X, n, l are considered.

Mn-Ni anti-site disorder					Ni 3d electron-electron correlation				
x	P_0 (%)	$P_{0_{\text{Ni}3d}}$ (%)	$P_{0_{\text{Mn}3d}}$ (%)	$P_{0_{\text{Ce}4f}}$ (%)	U_{Ni}	P_0 (%)	$P_{0_{\text{Ni}3d}}$ (%)	$P_{0_{\text{Mn}3d}}$ (%)	$P_{0_{\text{Ce}4f}}$ (%)
0	33.4	13.4	10.4	7	3	18.2	4.9	3.3	5.8
0.04	40	18.6	9.2	7.5	4	20.6	9.1	3.2	5.2
0.06	45	21.4	9.1	8.4	5	26.7	15	3	5.2
0.08	47	23.1	9.2	9.3	6	38.6	25.3	2.7	5.6
0.10	48.4	24.3	8.8	8.9	6.5	45	32.2	2.4	5.4
0.12	50.1	25.3	8.8	9	7	54	42	2	5.2

state properties. This is not in agreement with the spin polarization results we obtain here and so we discuss below the possible reason for this.

P_0 , being proportional to the difference of $n_{\downarrow}(E_F)$ and $n_{\uparrow}(E_F)$, is highly sensitive to any small change of the DOS at E_F . So, it is very unlikely that the states at E_F that are dominated by Ni 3d PDOS will not be influenced by U_{Ni} , whose value (6.5 eV) we find to be larger than U_{Mn} (4.5 eV) from the comparison of the experimental HAXPES VB with DFT calculations performed by us using SPRKKR. Our results clearly show that U_{Ni} has large influence on both the position of the VB peaks A and B (Fig. 2 of MS) as well as the DOS close to E_F (Fig. 3(d)). This leads to large increase of P_0 (Fig. 3b, Fig. S7 and Table I).

On the other hand, the spin polarized DOS near E_F with U_{Ni} was not shown in Ref.9. Fig. 4(b,c) of that work shows the total and $s, d,$ and f PDOS for $U_{\text{Mn}}=0$ and 6 eV. Based on this figure the authors conclude that P_0 increases from 10% to 30% with U_{Mn} increasing from 0 to 6 eV. We have analyzed this figure critically and find that the increase in P_0 in Ref. 9 is due to an unusual variation of Ce 4f PDOS at E_F for $U_{\text{Mn}}=6$. In their calculation, Ce 4f PDOS at E_F has a value of 0.3 for the minority spin, whereas in the majority spin PDOS it is largely reduced to 0.02. Thus, increase in P_0 to 30% for $U_{\text{Mn}}=6$ eV results primarily from the variation of the Ce 4f spin polarized states. Thus, we find $P_{0_{\text{Ce}4f}}$ (defined in Table I of SM) increases from 7.9% to 30%, a whopping 380% increase, while P_0 increases from 10 to 30%. Thus at $U_{\text{Mn}}=6$ eV, the whole spin polarization is contributed by Ce 4f states only.

The above discussed effect of U_{Mn} on P_0 and Ce 4f states is **unlikely**, since the Mn atom is surrounded by the Ni atoms and Ce is only the second nearest neighbor at a large distance of 3.02Å. Rather, one would expect that the Ni 3d states that are dominant at E_F would

contribute to P_0 , but between Fig. 4(b) and Fig. 4(c) of Ref. 9, the 3d states hardly change (for $U_{\text{Mn}}=0$ these are 0.3 and 0.5 states/eV for majority and minority spin, respectively and for $U_{\text{Mn}}=6$ eV these are 0.2 and 0.4 states/eV for majority and minority spin, respectively). Thus, strangely, $P_{0_{3d}}$ *i.e.* spin polarization due to the 3d states remains essentially similar ($P_{0_{3d}}=13\%$ for $U_{\text{Mn}}=0$ and $P_{0_{3d}}=16\%$ $U_{\text{Mn}}=6$ eV). Thus, while $P_{0_{\text{Ce}4f}}$ increases by 380%, $P_{0_{3d}}$ hardly changes. This seems to be an unphysical result.

We find that the increase of P_0 for both anti-site disorder (x) as well as electron-electron correlation of the Ni 3d electrons (U_{Ni}) is primarily due to the changes in the Ni 3d PDOS. Table I of SM clearly shows how only $P_{0_{\text{Ni}3d}}$ increases as P_0 , while $P_{0_{\text{Ce}4f}}$ and $P_{0_{\text{Mn}3d}}$ remain almost unchanged and thus do not play any role in the enhancement of P_0 . For comparison with Ref. 9, in Fig. S8, we show the total and PDOS with $U_{\text{Mn}}=6$ eV, with $U_{\text{Ni}}=U_{\text{Ce}}=0$. We find that P_0 decreases from 33.4% to 13.2% with U_{Mn} varying from 0 to 6 eV (Fig. 4(a) in MS). It is evident that the total f PDOS is less than the total d PDOS over the entire range and most importantly remains similar between $U_{\text{Mn}}=0$ and $U_{\text{Mn}}=6$ eV. Thus, $P_{0_{4f}}$ is almost unchanged (rather decreases slightly) from 7.3% to 5.3% from $U_{\text{Mn}}=0$ to 6 eV. This is in stark disagreement with the 380% increase of $P_{0_{4f}}$ that can be concluded from Ref.⁹.

B. SD2: Surface valence transition

The Ce 3d core-level spectrum displays two sets of triplet peaks corresponding to the spin-orbit split components (Fig. S9). The most intense among the triplet peaks is the f^1 satellite associated with a poorly screened $3d^9 4f^1$ final state occurring at 902.8 eV and 884.4 eV binding energies. The two additional satellite peaks that

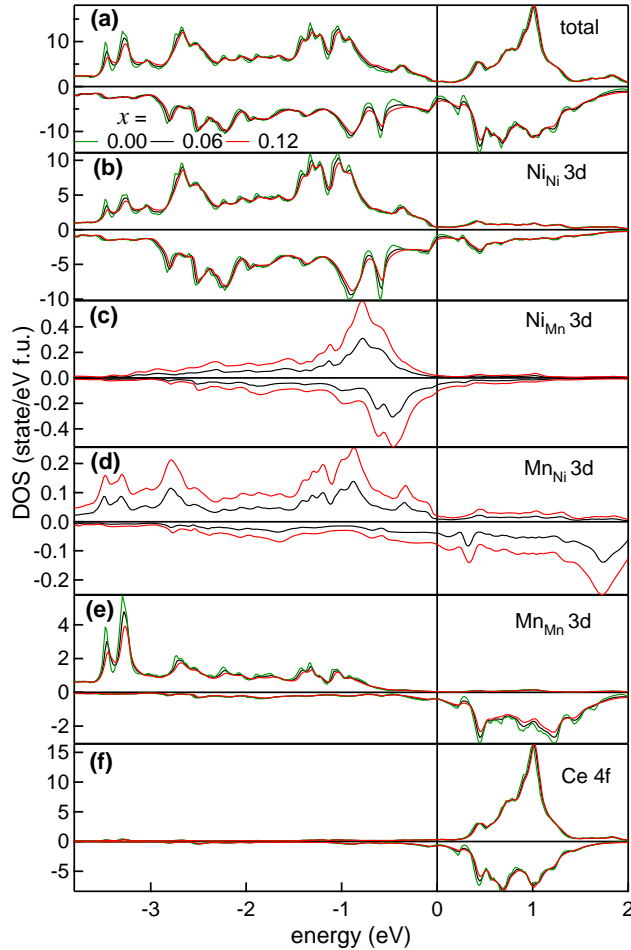


Fig. S 2: Spin polarized (a) total DOS and the PDOS for (b) Ni_{Ni} 3d, (c) Ni_{Mn} 3d, (d) Mn_{Ni} 3d, (e) Mn_{Mn} 3d and (f) Ce 4f as a function of Mn-Ni anti-site disorder quantified by $x = 0, 0.06$ and 0.12 .

occur at relatively higher and lower binding energies are referred to as f^0 and f^2 , respectively. The well screened f^2 satellite has an extra screening electron with $3d^9 4f^2$ final state, while the f^0 satellite is related to $3d^9 4f^0$ final state^{22,23}. Notable in Fig. S9 is the large f^0 intensity in HAXPES, which decreases drastically in soft x-ray PES (XPS). In order to extract quantitative information, the Ce 3d core-level spectra were fitted using a least square error minimization routine with each peak assigned a Doniach and Šunjić (DS) line shape²⁴. This was further convoluted with a Gaussian function of fixed width to represent the instrumental broadening. Since Ni 2p that appears close in binding energy to Ce 3d might contribute to the intensity in the Ce 3d region, the Ni 2p main and satellite peaks were also included in the fitting scheme. The whole region including Ni 2p along with the components is shown in Fig. S10. A total 10 DS line shapes were used, 6 for Ce 3d comprising of the three f^n components for each spin-orbit (s.o.) peaks and 4 for Ni 2p

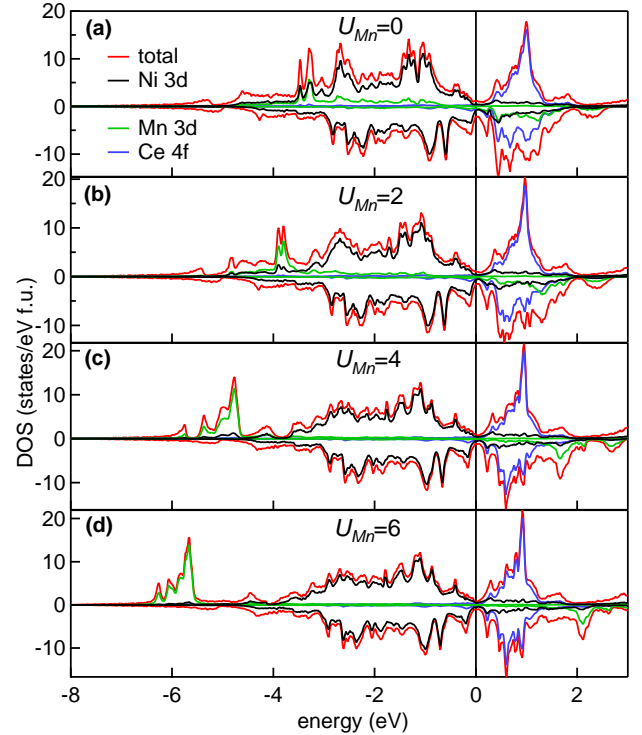


Fig. S 3: Spin polarized total DOS and Ni 3d, Mn 3d and Ce 4f PDOS as a function of U_{Mn} with $U_{Ni} = U_{Ce} = 0$ where for (a) $U_{Mn} = 0$ eV, (b) $U_{Mn} = 2$ eV, (c) $U_{Mn} = 4$ eV, and (d) $U_{Mn} = 6$ eV.

representing the main peak and satellite for both the s.o. components. The parameters defining each DS line shape are the intensity, position, width (Γ) and asymmetry parameter (α). A Tougaard background was also included in the fitting scheme, where the B_1 parameter was varied and the C parameter was kept fixed at 1643 eV^{225} . Thus, a total of 35 parameters defined the full spectral shape including Ce 3d and Ni 2p. However, some reasonable constraints were needed, for example (i) the life time broadening of f^0 for Ce $3d_{3/2}$ was constrained to be greater than or equal to f^0 for Ce $3d_{5/2}$, (ii) α was kept equal for all Ce 3d DS components, (iii) for XPS fitting, the satellites of Ni 2p have same width as HAXPES.

From the least square fitting, we find that the normalized intensity of f^0 ($I_n(f^0)$) is 0.15 for HAXPES, where $I_n(f^0) = I(f^0) / \sum_{n=0}^2 I(f^n)$ (Table II of SM). Such large intensity of f^0 having almost similar height as f^1 is unusual and has not been observed in other Ce based intermetallic compounds^{26,27}. In contrast, $I_n(f^0)$ is an order of magnitude less (0.04) in XPS. This could be related to the bulk sensitivity of HAXPES with mean free path (λ) of 91 \AA for Ce 3d electrons while XPS is surface sensitive with $\lambda = 13 \text{ \AA}$ ²⁸. In order to understand the differences between the above discussed bulk and sur-

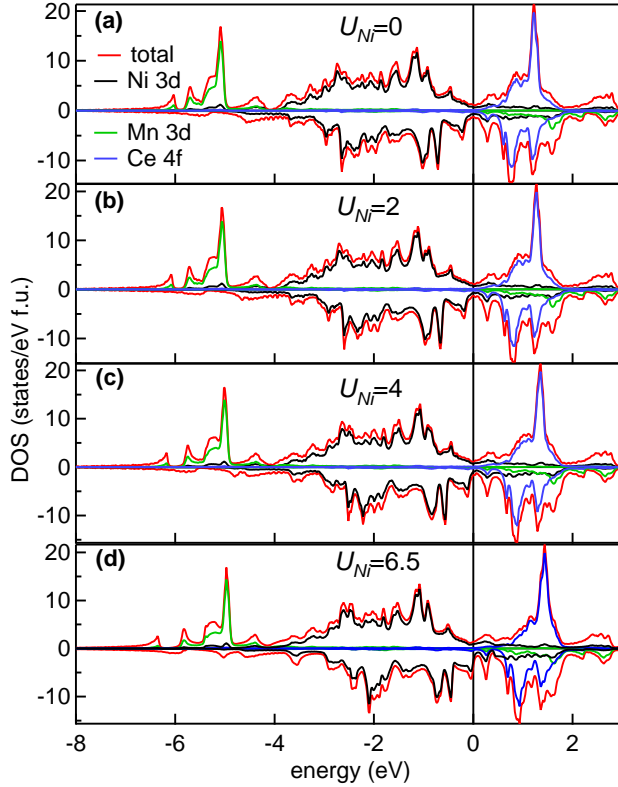


Fig. S 4: Spin polarized total DOS and Ni 3d, Mn 3d and Ce 4f PDOS as a function of U_{Ni} with fixed $U_{Mn} = 4.5$ eV and $U_{Ce} = 7$ eV where for (a) $U_{Ni} = 0$ eV, (b) $U_{Ni} = 2$ eV, (c) $U_{Ni} = 4$ eV and (d) $U_{Ni} = 6.5$ eV.

face Ce 3d spectra, we turn to a simplified version of the Anderson single-impurity model²¹ proposed by Imer and Wuilloud (IW), where the extended valence states are considered as a band of infinitely narrow width¹¹. The Ce 3d spectrum is calculated as a function of the energy of the unhybridized 4f state relative to E_F (ϵ_f), Coulomb repulsion between 4f electrons at the same site (U_{ff}), Coulomb attraction between 4f electron and the final-state core hole (U_{fc}), and hybridization between the 4f states and the conduction band (Δ).

The above mentioned parameters are varied such that the f^n satellites of the calculated Ce $3d_{3/2}$ spectrum have similar intensities (I_n) and energy separations between f^0 and f^n (δ_{0n}), as obtained from the fitting of the experimental spectra. For example, besides the large change in $I_n(f^0)$, the binding energies of the f^n satellites are lower in HAXPES (this is not due to recoil effect¹, see Fig. S11), resulting in different δ_{0n} as shown in Table II.

In order to simulate the Ce 3d HAXPES spectra using IW theory, we note that $I_n(f^0)$ increases sensitively with ϵ_f , and so this parameter is varied keeping the others fixed at the values suggested for Ce compounds ($\Delta = 1.5$ eV, $U_{ff} = 7$ eV, $U_{fc} = 10$ eV)¹¹. For $\epsilon_f = -1$ eV,

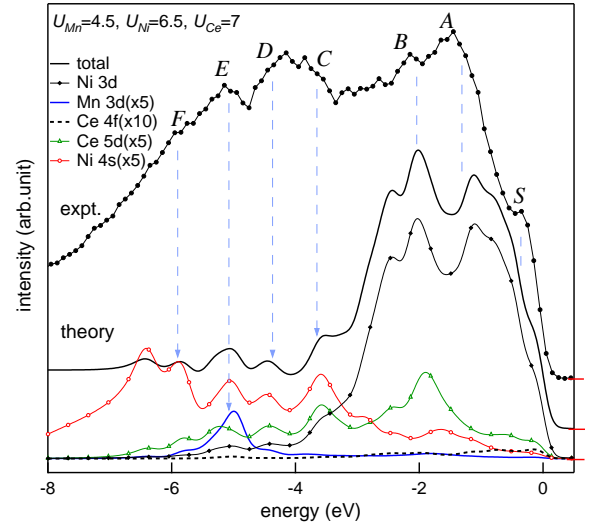


Fig. S 5: The calculated valence band spectrum for $U(4.5,6.5,7)$ with the partial contributions from Ni 3d, Mn 3d, Ni 4s, Ce 5d and Ce 4f compared with experimental HAXPES VB spectrum. The spectra are staggered along the vertical axis, and the zero for each are shown on the right vertical axis by red horizontal lines. The peaks in the VB are marked by S, A, B, C, D, E and F. Light blue dashed arrows show the corresponding partial contributions to these features. A and B originates primarily from Ni 3d like states with small amount of contribution from Ce 5d and Ni 4s in B. Mn 3d along with Ni 4s like states show major contribution to E. C and D are related to Ni 4s, Ce 5d and Ni 3d. Features F and S mainly originate from Ni 4s and Ni 3d, respectively. The disagreement in the intensity between experiment and theory could be related to the inelastic background that is not considered in the latter.

we find $I_n(f^0) = 0.15$ in excellent agreement with experiment; and the other quantities such as δ_{0n} , $I_n(f^1)$ and $I_n(f^2)$ are also in good agreement (Table II). The calculated spectrum obtained with $\epsilon_f = -1$ eV, $\Delta = 1.5$ eV, $U_{ff} = 7$ eV, $U_{fc} = 10$ eV is shown at the bottom of Fig. S9(a), where the f^n satellites have been broadened by their respective widths obtained from the fitting and a background²⁵ has also been added. The f occupancy in the ground state (n_f) turns out to be 0.8, indicating a mixed valent state with 20% Ce in f^0 (Ce^{4+}) while 80% in f^1 (Ce^{3+}) configuration.

In order to simulate the Ce 3d XPS spectrum, we decrease ϵ_f to -2.5 eV from the HAXPES value of -1 eV and obtain $I_n(f^0) = 0.04$. But concomitantly, both δ_{01} ($=12.1$ eV) and δ_{02} ($=18.9$ eV) become larger than experimental values of 10.2 eV and 14.4 eV, respectively (Table II). In order to decrease δ_{0n} , both Δ and U_{fc} need to be decreased, and thus, we obtain a good agreement with experiment for $\epsilon_f = -2.5$ eV, $\Delta = 1.1$ eV, $U_{fc} = 8$ eV, and $U_{ff} = 7$ eV (bottom of Fig. S9(b)). Due to the decrease of ϵ_f , n_f increases to 0.98, and thus, in contrast to bulk, at the surface Ce has predominantly $3d^9 4f^1$ (Ce^{3+})

TABLE II: The parameters for Ce $3d_{3/2}$ such as normalized intensity $I_n(f^n)$, binding energy (E_B), energy separation δ_{0n} between f^n satellites obtained from least square fitting compared with those obtained from IW theory. All the values are in eV and $U_{ff} = 7$ eV in both cases. The error in $I_n(f^0)$ is significantly smaller because the f^0 satellite it is well separated in energy from all the other components.

$h\nu$ (keV)	f^n	PES experiment			IW theory				
		I_n	$E_B \pm 0.2$	$\delta_{0n} \pm 0.4$	ϵ_f	Δ	U_{fc}	I_n	δ_{0n}
8	f^0	0.15 ± 0.01	913.5	0				0.15	0
	f^1	0.6 ± 0.1	902.8	10.7	-1.0	1.5	10	0.53	10.5
	f^2	0.25 ± 0.1	897.8	15.7				0.32	16.1
1.48	f^0	0.04 ± 0.01	914.3	0				0.04	0
	f^1	0.5 ± 0.1	904.1	10.2	-2.5	1.1	8	0.62	10.1
	f^2	0.45 ± 0.1	899.9	14.4				0.34	14.7

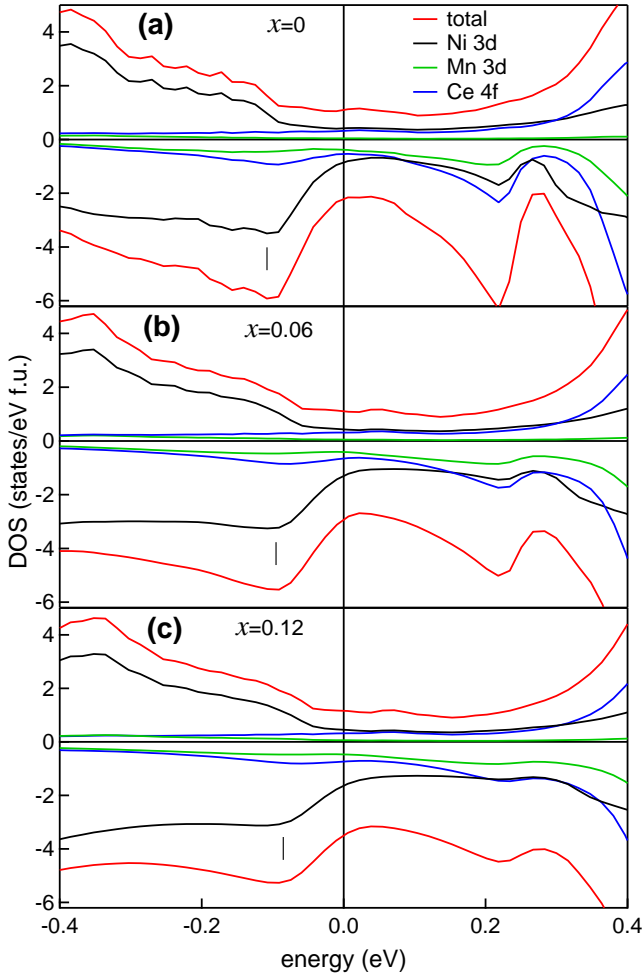


Fig. S 6: Spin polarized total, Ni 3d, Mn 3d and Ce 4f PDOS in a small range around E_F , as a function of anti-site disorder (a) $x = 0$, (b) $x = 0.06$ and (c) $x = 0.12$.

ground state. Thus, in the bulk, since ϵ_f ($= -1$ eV) is closer to E_F and Δ is larger, the Ce 4f electron transfers to the valence states comprising of primarily Ni 3d states making CeMnNi_4 a mixed valent system with 4f

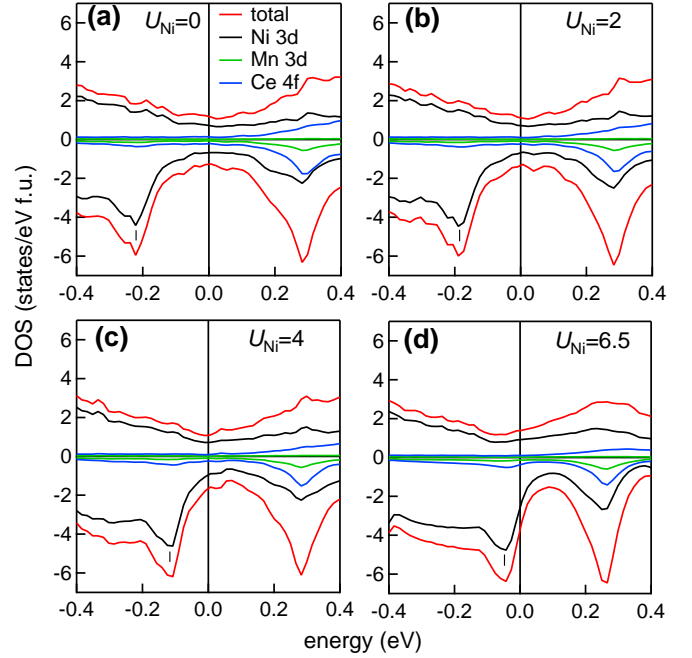


Fig. S 7: Spin polarized total, Ni 3d, Mn 3d and Ce 4f PDOS in a small range around E_F , as a function of U_{Ni} with $U_{Mn} = 4.5$ eV and $U_{Ce} = 7$ eV for $U_{Ni} =$ (a) 0 eV, (b) 2 eV, (c) 4 eV and (d) 6.5 eV. The black ticks show the position of Ni 3d minority spin peak that shifts towards E_F with U_{Ni} .

occupancy of $n_f = 0.8$. However, at the surface, the reduced hybridization between the Ce 4f and unsaturated 3d states results in a lowering of the Ce 4f states further below E_F . This increases the occupancy of the Ce 4f level ($n_f = 0.98$) and results in the surface valence transition. Decrease in U_{fc} from about 10 eV to 8 eV at the surface is also a manifestation of this transition possibly caused by the more efficient screening of the core hole due to increased n_f .

It might be noted that although the surface valence transition is clearly manifested in the Ce 3d core-level spectra, it does not however result in appearance of any Ce 4f peak in the XPS VB (Fig. S12), which could be

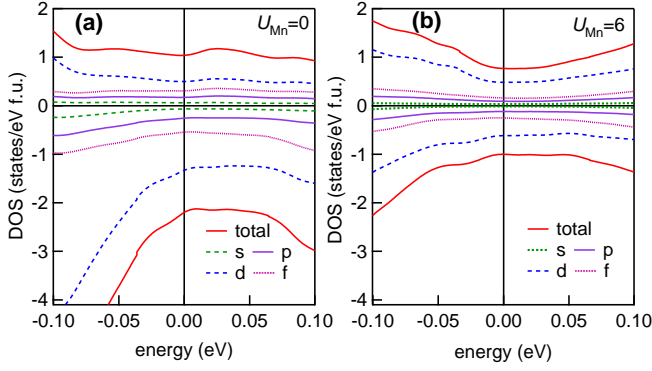


Fig. S 8: Spin polarized total DOS and total s , p , d and f PDOS of CeMnNi₄ with (a) $U_{Mn}=0$ eV (b) $U_{Mn}=6$ eV for comparison with Fig. 4(b,c) of Ref. 9.

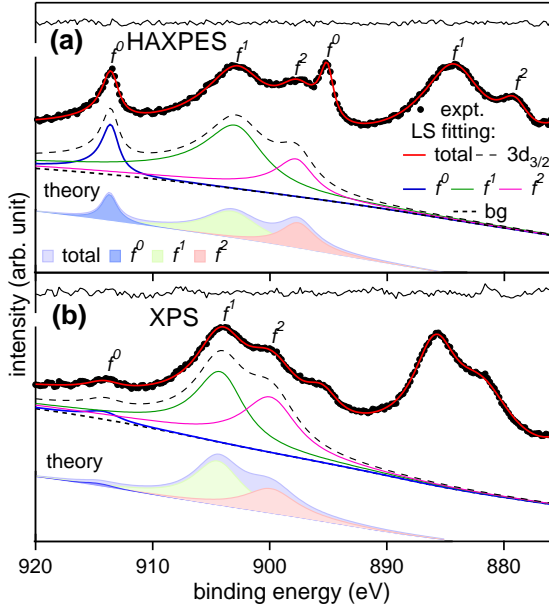


Fig. S 9: Ce $3d$ core-level spectra (black dots) recorded with (a) 8 keV (HAXPES) and (b) 1.48 keV (XPS) photon energies. The spectra have been fitted (red line) using a least square (LS) error minimization routine and the f^n satellite components for Ce $3d_{3/2}$ are shown. The calculated Ce $3d_{3/2}$ spectra using IW theory along with the f^n satellites are shown at the bottom and the residuals of fitting (black line) are shown at the top of each panel.

expected due to enhanced n_f at the surface. Firstly, this happens because the occupied part of Ce $4f$ PDOS from -3 eV to E_F is largely diminished, broad and featureless

(Fig. S13). Its integration (blue line) up to E_F gives $n_f = 0.96$ in the bulk from DFT, which is in reasonable agreement with $n_f = 0.8$ from IW method, considering the assumptions of the latter model calculation¹¹. The increase of n_f by 0.18 at the surface obtained from IW

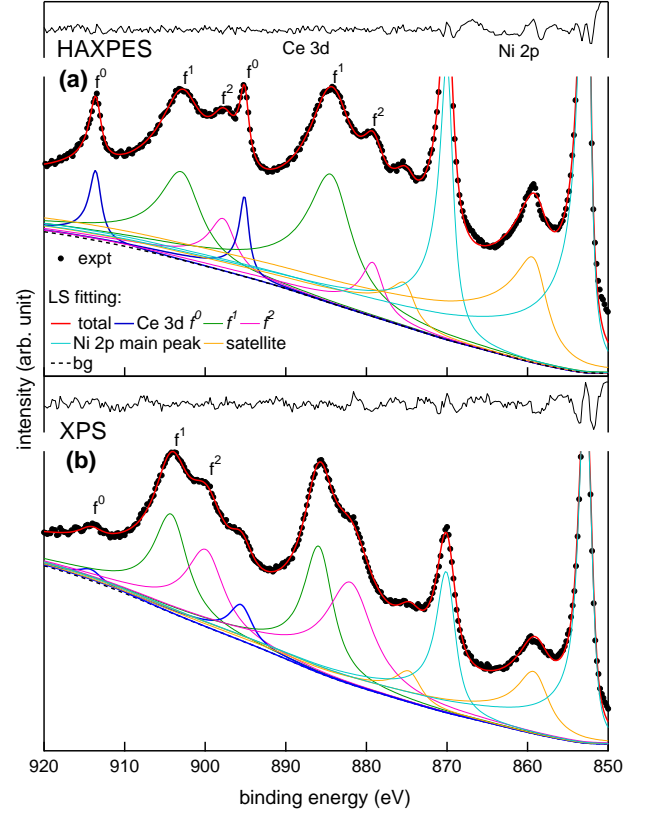


Fig. S 10: Ce $3d$ core-level spectra (black circles, includes Ni $2p$ region) with (a) HAXPES compared with (b) XPS. The spectra has been fitted (red line) using a least square (LS) error minimization routine, and the residuals (black line) are shown at the top of each panel. The different components such as Ce $3d$ f^0 , f^1 , and f^2 , Ni $2p$ main peaks and satellites as well as a Tougaard background are shown.

method would manifest itself through a small shift of the Ce $4f$ PDOS by 0.25 eV (obtained from integration of PDOS that gives $n_f = 1.14$) to lower energy in the rigid band model (red dashed line in Fig. S13). Thus, the main peak of Ce $4f$ still remains above E_F at the surface. Secondly, occupied Ni $3d$ PDOS as well as its photoemission cross-section¹⁶ are much larger than Ce $4f$ (Fig. S12, S2-S4) resulting in complete domination of the VB by Ni $3d$ states at low photon energies too. This is reconfirmed by the relative contributions of Ni $3d$ and Ce $4f$ to the calculated XPS VB in Fig. S12.

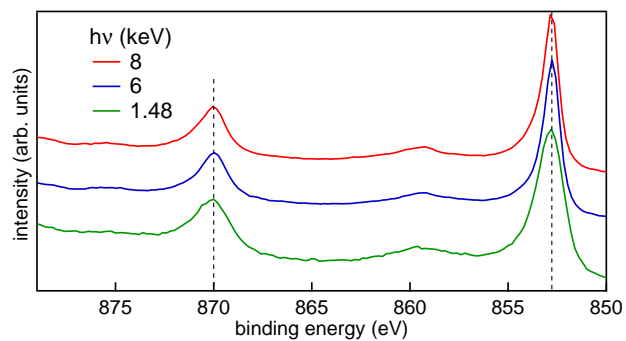


Fig. S 11: Ni $2p$ core level spectra of CeMnNi_4 using 8, 6 and 1.48 kV photon energies, normalized to same height at the Ni $2p_{3/2}$ peak and staggered along the vertical axis for clarity of presentation. The recoil effect that has been observed in the HAXPES spectra of light materials¹ is absent here since it comprises of heavier $3d$ and rare earth elements. The recoil effect, if present causes a uniform shift of the peaks to higher binding energies that increases with the kinetic energy of the electrons, which in turn depends on the photon energy used. We confirm the absence of any recoil effect here from the Ni $2p$ spectra taken with different photon energies where any shift of the peaks for different photon energies is absent.

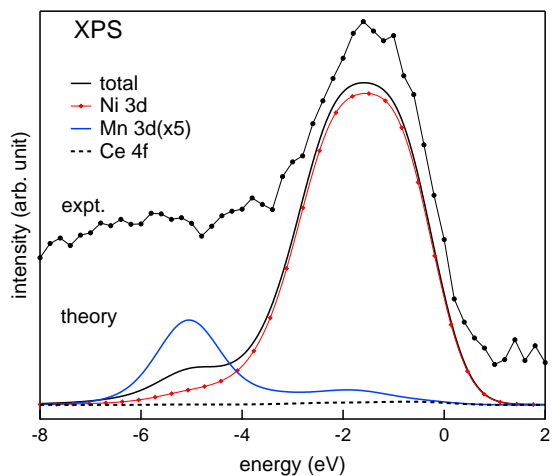


Fig. S 12: The XPS valence band spectrum of CeMnNi_4 taken with 1.25 keV photon energy (black line with dots) compared with calculated VB along with the Ni $3d$, Mn $3d$ ($\times 5$) and Ce $4f$ partial contributions.

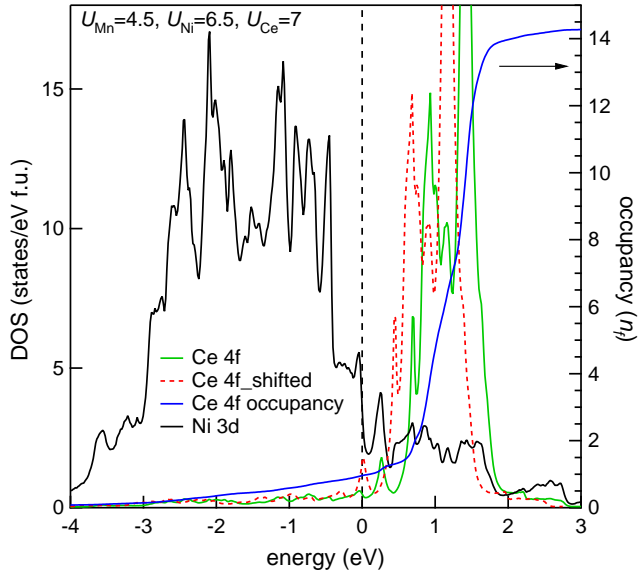


Fig. S 13: Spin integrated Ni 3d and Ce 4f PDOS for CeMnNi₄ with optimum $U(4.5, 6.5, 7)$. The integration of the Ce 4f PDOS (blue line) that shows the occupancy (n_f) on the right axis.